

Metastability in individual magnetic vortices

D. García-Pons,¹ J. Pérez-Bailón,¹ A. Méndiz,¹ V. Júlvez,¹ M. Hack,² K. Wurster,² R. Kleiner,² D. Koelle,² and M. J. Martínez-Pérez¹

¹*Instituto de Nanociencia y Materiales de Aragón (INMA), CSIC-Universidad de Zaragoza, Zaragoza, Spain*

²*Physikalisches Institut, Center for Quantum Science (CQ) and LISA⁺, Universität Tübingen, Auf der Morgenstelle 14, 72076 Tübingen, Germany*

(*Electronic mail: pemar@unizar.es)

(Dated: 28 October 2024)

Magnetic nanoparticles play a crucial role in different fields such as biomedicine or information and quantum technologies. These applications require nanoparticles with a single, well-defined energy minimum, free of metastable states, and characterized by narrow switching field distributions. Here, we demonstrate that high-transition-temperature nanoSQUIDs can be successfully applied to the characterization of individual nanodiscs hosting magnetic vortices. We present measurements performed under varying temperature and external magnetic field, revealing signatures of ubiquitous, multiple metastable configurations. We also demonstrate that metastability can be reduced by introducing an intended asymmetry. NanoSQUID measurements can be applied to optimize the fabrication of on-demand spin-texture states, such as degenerated vortices or particles with fixed circulation and deterministic and narrow switching probabilities.

Magnetic vortices^{1,2} arise in confined ferromagnets as a result of the balance between magnetostatic and exchange energies: magnetization curls in plane with defined circulation, forming a vortex core pointing out of plane with up or down polarity. Magnetic vortices have been extensively investigated for applications in spintronics due to their stable non-uniform magnetization (e.g., as logic units^{3–6} or to induce superconducting correlations in ferromagnets through the proximity effect^{7,8}) and due to their rich dynamical behavior in the sub-GHz and GHz range (e.g., as spin-torque nano-oscillators^{9–11} or as spin-wave emitters¹²). Despite this amount of interesting physics, quantum properties of magnetic vortices arising at very low temperatures are largely unknown. Looking at quantum technologies, magnetic textures confined in nanoscopic magnets are attracting much attention in the growing field of cavity magnonics^{13–15}. Domain walls, vortices and skyrmions are topological solitons that can be used to encode quantum states^{16–20}. Magnetic vortices have also been recently proposed as nanoscopic electron paramagnetic resonance sensors capable of reaching single spin sensitivity²¹. Additionally, vortices could potentially serve to increase the weak interaction between superconducting microcircuits and spin qubits, even achieving the challenging regime of strong spin-photon coupling²². For the development of these applications, it is important to obtain nanomagnets with well-defined spin-texture ground states and deterministic and narrow switching distributions, while minimizing metastability as much as possible^{23,24}.

In this work, we show the characterization of individual spin textures stabilized in permalloy (Py, Ni₈₀Fe₂₀) discs. For this, we use nanoscopic Superconducting Quantum Interference Devices^{25,26} (nanoSQUIDs) based on the high-transition-temperature and high-critical-field cuprate superconductor YBa₂Cu₃O₇ (YBCO), operative at variable temperature and under sweeping magnetic fields^{27–29}. On the one hand, we identify the nucleation, displacement and annihilation of the vortex core. On the other, we can also distinguish between clockwise (CW) and counterclockwise (CCW) circu-

lation states. Even more important, the occurrence of different metastable states with similar magnetic configuration at certain temperature ranges is experimentally accessible.

NanoSQUID fabrication and operation is described elsewhere^{27–30}. In short: a thin film of YBCO is grown epitaxially using pulsed laser deposition on a SrTiO₃ (STO) [001] bicrystal substrate, with a 24° grain-boundary misorientation. This structural boundary translates into a YBCO grain boundary Josephson junction (GBJ)³¹. After pre patterning by photolithography and Ar ion milling, nanoSQUIDs are patterned by Focused Ion Beam (FIB) milling with 30-keV Ga ions, defining a superconducting loop intersected by two GBJs. Additionally, an evaporated Au layer on top of the YBCO film is used as a resistive shunt to ensure nonhysteretic current-voltage characteristics of the GBJs and to minimize Ga implantation into the YBCO film and excessive heating during FIB milling.

Fabrication and transport of the Py discs is described in the following. A 40-nm-thick Py film is deposited by e-beam evaporation onto a 200-nm-thick free-standing silicon nitride membrane (PELCO© support films for transmission electron microscopy with lateral size of 100 μm × 100 μm). The disc perimeter is defined by Ga-FIB milling using a low ion current of 10 pA to maximize resolution. Note that Ga ions also partially etch the Si₃N₄ layer underneath the Py film (Figure 1a). A larger area of the Py film is then removed by FIB-milling with a higher current of 280 pA (panel b). The entire sample is flipped upside down, and a palette is patterned by Ga-FIB milling (panel c). The Omniprobe needle is attached using a small (focused electron beam induced) deposit of Pt (panel d). The palette is then completely removed and lifted from the remaining silicon nitride membrane (panel e). Subsequently, the palette is approached to the sensor by combining electron and ion beam imaging to precisely control the distance between the palette and the nanoSQUID (panels f and g). The disc position is chosen to optimize the inductive coupling to the nanoSQUID loop^{27,32}. Finally, two small Pt deposits are used to fix the palette position (panel h), and the remaining part of

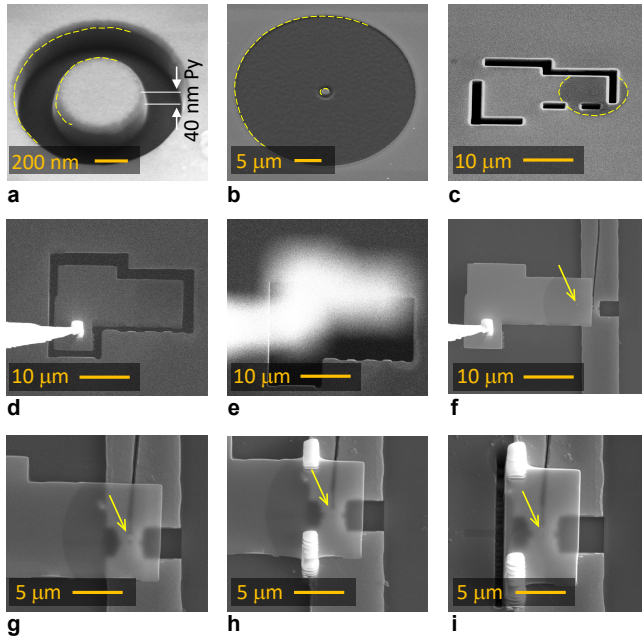


FIG. 1. Scanning electron microscopy (SEM) images showing the disc fabrication and transport (see text). The border between the Py film and the Si_3N_4 membrane is marked with a dashed yellow line in panels a-c. The Py disc is highlighted by a yellow arrow in panels f-i.

the palette is removed to eliminate any excess Py film (panel i). Results presented here are obtained with four different Py nanodiscs shown in Figure 2a. Disc1 has a maximum diameter of 600 nm and a flat side that breaks symmetry, whereas disc2 (diameter of 580 nm), disc3 (diameter of 490 nm) and disc4 (diameter of 650 nm) are nominally perfectly circular.

Measurements are performed in a variable temperature inset ($1.4 \text{ K} < T < 80 \text{ K}$) with a superconducting magnet. The nanoSQUID sensor can be aligned with respect to the external magnetic field \vec{B} by means of a rotator. In this way, no magnetic flux is coupled to the Josephson junctions, neither to the nanoSQUID (operated in flux-locked loop mode). Hysteresis loops are obtained by sweeping B while monitoring the SQUID output voltage. The latter is proportional to the total magnetic flux Φ coupled to the nanoSQUID by the stray magnetic field from the Py disc, i.e., this signal is proportional to the magnetization.

Figure 3b shows a typical hysteresis loop measured at $T = 70 \text{ K}$ for disc1, with \vec{B} parallel to the flat side (as shown in the inset of panel a). At $B = 0$ the disc is in a vortex state, which produces a very small stray field and, therefore, no net flux coupled to the SQUID. When B is raised, the vortex is displaced perpendicularly to the magnetic field, yielding a linearly increasing flux coupled to the SQUID. At small B , the vortex displacement is reversible but, when the field exceeds a certain threshold, the vortex is expelled out of the disc. This results in the sudden collapse of the magnetization into a saturated state at the annihilation field B_a . If the magnetic field is reduced from saturation, the vortex state arises again at the nucleation field (typically different from B_a), resulting in

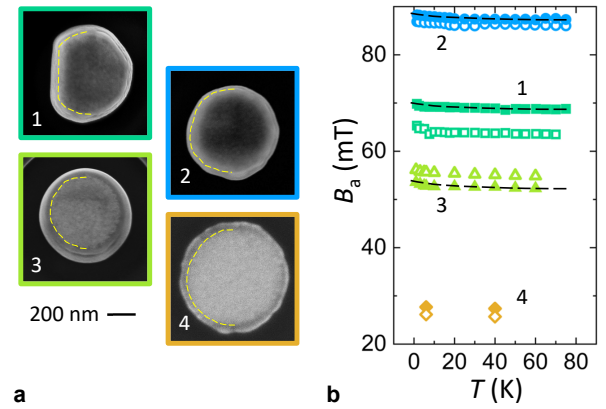


FIG. 2. a: SEM images of the samples. Yellow dashed lines highlight the perimeter of the Py discs over the Si_3N_4 membranes. b: Average positive annihilation fields measured for full loops ($B_a^{+\text{full}}$, filled scatter) and semi-loops (B_a^+ , empty scatter). Dashed lines are a guide to the eye to highlight the temperature dependence.

two hysteretic lobes representative for vortex magnetization reversal³³.

Vortex nucleation is a complex phenomenon, often preceded by the formation of curved magnetization configurations or even two-vortex states³⁴. This behavior usually leads to the observation of multiple steps in the hysteresis curve, that complicate analysis³⁵. For this reason, we will focus exclusively on the phenomenon of vortex annihilation and the experimentally observed annihilation fields. We perform three types of measurements, summarized in Figure 3: (a) half-loops from zero to negative annihilation field B_a^- ; (b) full-loops showing transitions to both positive and negative saturation states at $B_a^{+\text{full}}$ and $B_a^{-\text{full}}$, respectively; and (c) half-loops from zero to the positive saturation field, where vortex expulsion occurs at B_a^+ . Measurements are repeated for all discs at varying temperatures. The positive annihilation fields for half- and full-cycles is determined and shown in Figure 2b. As indicated by the dashed lines (used as a guide for the eye), $B_a(T)$ follows a logarithmic dependence^{36–38}. This behavior is well-known and expected from a thermally activated process over an energy barrier, such as vortex annihilation^{35,39–43}. What is notable is the fact that $B_a^+ \neq B_a^{+\text{full}}$ for all discs and across the entire temperature range accessible experimentally. The same behavior is emphasized in panels d-f in Figure 3.

To understand this, let us first focus on disc1, with a flat side parallel to the externally applied magnetic field (see Figure 3a). In perfectly circular discs, both vortex circulation and polarity states are degenerated. The degeneracy can be easily broken by introducing some asymmetry, such as a flat side⁴⁴. Under such circumstances, the probability of the vortex nucleating near the flat side will be higher due to the larger demagnetizing field. When this happens at positive B (Figure 3e and f), this process will always yield a CW rotating vortex. In contrast, vortex nucleation at negative fields will yield a CCW configuration (Figure 3d and r). Interestingly, the circulation will, in turn, fix the direction of the vortex displacement under sweeping B , determining the side where vortex expul-

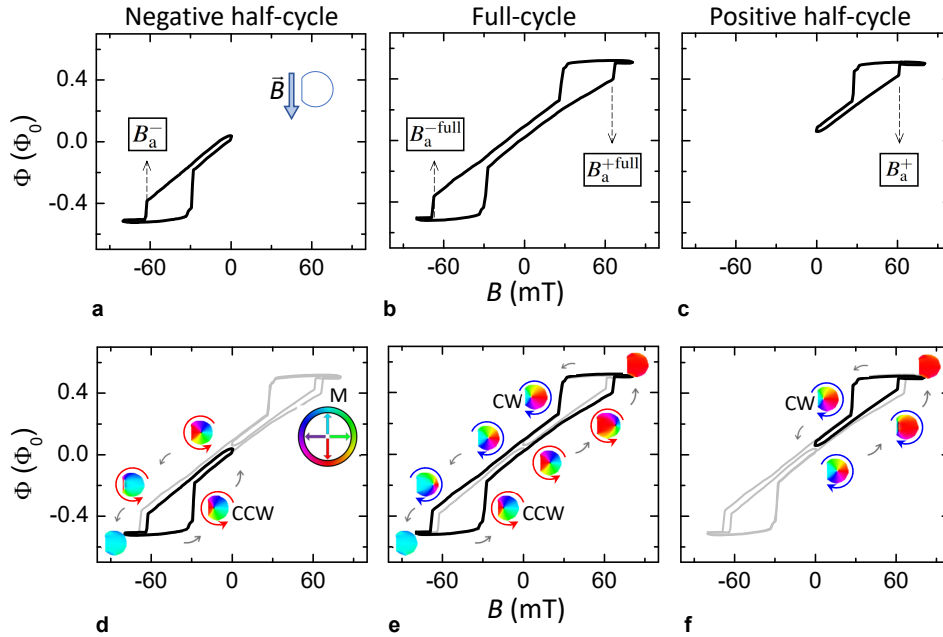


FIG. 3. Experimental full and half magnetization cycles $\Phi(B)$ measured for disc1 at $T = 70$ K. The field is always applied parallel to the flat side of the particle (see inset in panel a). Vertical axes are given in units of flux coupled to the nanoSQUID loop (Φ_0 is the flux quantum). This is proportional to the nanoSQUID output voltage and, therefore, to the sample magnetization. Annihilation fields B_a^- , B_a^{-full} , B_a^{+full} and B_a^+ are indicated in panels a-c by vertical dashed arrows. Panels d-f show each hysteresis loop (black curve) alongside the others (grey curves) to highlight the differences between full- and half-cycles. The magnetization configuration is simulated with Mumax and shown at certain field values following the sequence indicated by the small grey arrows (see the magnetization legend in panel d). Red and blue circular arrows highlight the sense of circulation for CCW and CW directions, respectively.

sion occurs. The annihilation fields will be slightly different depending if expulsion takes place from the flat or the round side of the disc. This is to say, annihilation fields will depend on the circulation, providing an easy method to measure the vortex's direction of rotation.

This effect has been experimentally observed, by measuring half- and full-hysteresis loops in arrays⁴⁵ and pairs of nanodiscs⁴⁶. Full cycles result in vortex nucleation and annihilation at opposite sides of the disc, whereas half cycles cause the vortex to nucleate and annihilate at nearby locations. This is to say, vortex annihilation in the half-cycles will always occur near the flat side, where its demagnetization energy is higher and, therefore, will take place at lower magnetic fields. On the other hand, annihilation in the full-cycles will take place near the curved side, with lower demagnetization energy, and thus will happen at slightly higher fields. In other words, $|B_a^-| < |B_a^{-full}|$ and $B_a^+ < B_a^{+full}$. These phenomena are fully visible in the measurements shown in Figure 3 and summarized in Figure 2b for variable temperature. To better illustrate this effect we also perform micromagnetic simulations using MuMax3^{47,48} considering the shape of disc1 as determined from the SEM images and typical material parameters for Py⁴⁹. Results from the simulations are shown in Figure 3d-f.

Notably, disc2, disc3 and disc4 also exhibit different annihilation fields for full- and half-cycles (Figure 2b). This is probably due to the fact that unintended sample imperfections such as deviations from perfect circular shape, edge roughness

or inter-grain boundaries can also break the symmetry^{50,51}. This might also determine the direction of circulation and, therefore, the magnetization configuration before vortex annihilation. Unlike the disc with a flat side, in these cases we cannot easily predict the position of vortex nucleation and, therefore, the direction of circulation. Disc3 is particularly intriguing because, contrary to intuition, $|B_a^-| > B_a^{-full}$ and $B_a^+ > B_a^{+full}$. This is interesting since the vortex is typically nucleated close to the region with maximum energy. During the half-cycles, the vortices nucleate and annihilate near the same location, so we would expect $|B_a^-| < B_a^{-full}$ and $B_a^+ < B_a^{+full}$. However, annihilation does not occur from exactly the same magnetization configuration as nucleation. It is possible for the vortex to become trapped in a lower-energy metastable state. When this happens, vortex expulsion is less favourable, resulting in a higher annihilation field. A similar behavior has been observed in asymmetric discs such as disc1 when the external field is applied at intermediate angles with respect to the flat side⁴⁵.

As previously discussed, ideal vortex states are four-fold degenerate in circulation and polarity. Imperfections and asymmetries break this degeneracy but also allow for the stabilization of very similar vortex states, either with nearly identical magnetization configurations or with the vortex pinned at slightly different positions^{51,52}. These differences result in variations in the corresponding annihilation fields. NanoSQUID measurements on individual discs enable us to distinguish the nucleation of these metastable states and their

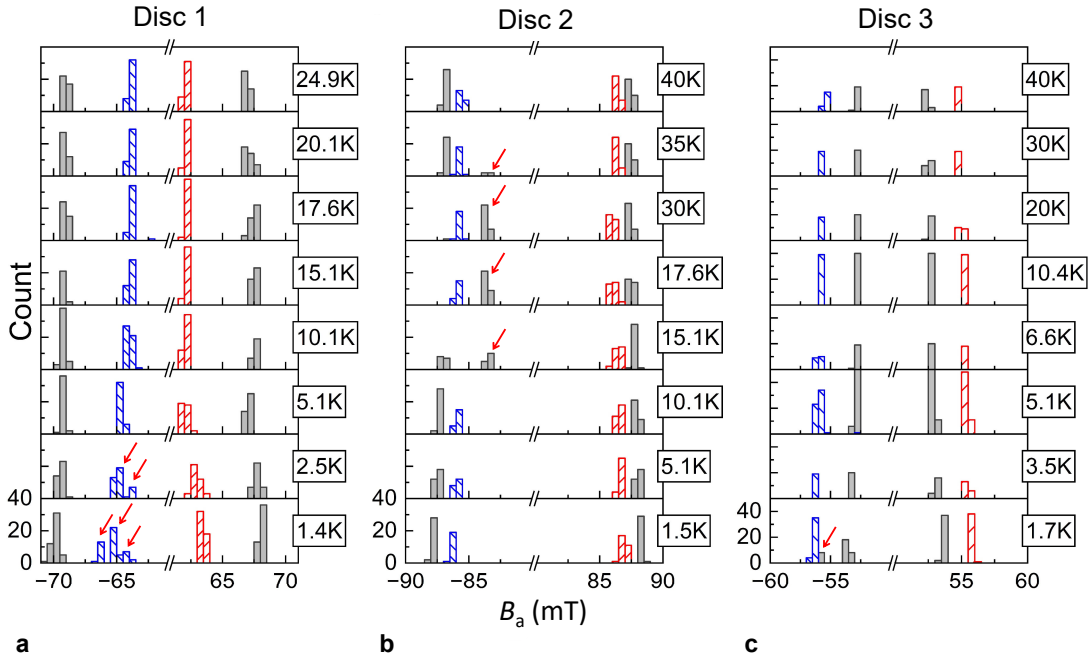


FIG. 4. Histograms of annihilation fields obtained from 40-50 repetitions at different temperatures given in the legend. Filled bars represent data extracted from full magnetization cycles ($B_a^{-\text{full}}$ and $B_a^{+\text{full}}$); while hatched blue bars (B_a^-) account for negative semi-loops, and hatched red bars (B_a^+) correspond to positive semi-loops. Small red arrows highlight signatures of metastability in all discs (see text).

relative probabilities, which depend not only on the sample quality but also on the temperature. To further explore this behavior we repeat each hysteresis measurement 40-50 times and make histograms of annihilation fields for half- and full-cycles. Results corresponding to disc1, disc2 and disc3 at different temperatures are shown in Figure 4.

Disc1 behaves as expected, with $|B_a^-| < |B_a^{-\text{full}}|$ and $B_a^+ < B_a^{+\text{full}}$ at all temperatures. On the other hand, B_a^- broadens as temperature decreases, even splitting into two (or more) multiple states at the lowest temperatures below 5 K (highlighted with arrows). This is a signature of metastability. Different annihilation fields result from slightly different magnetization configurations, each occurring with a certain probability. The height and shape of the annihilation histogram depend on the probability distribution of non-identical metastable configurations. We recall that, ideally, the mechanism for vortex expulsion should be equal for both positive and negative half-cycles. However, the fact that B_a^+ does not exhibit signatures of metastability suggests that the annihilation mechanism is different for CW and CCW configurations.

Disc2 and disc3 are even more complex. For example, below 15 and above 35 K, disc2 is characterized by well defined values of $B_a^{+\text{full}}$ and $B_a^{-\text{full}}$. On the other hand, at temperatures between 15 to 35 K, $B_a^{-\text{full}}$ splits into two distinct states; at 15.1 K both states share similar probability. Interestingly, one of these two states (highlighted with an arrow) annihilates at fields smaller than the corresponding B_a^- (just as disc3). Disc3 exhibits quite narrow distributions of the annihilation fields, always keeping $|B_a^-| > |B_a^{-\text{full}}|$ and $B_a^+ > B_a^{+\text{full}}$. Interestingly, at the lowest temperature $T = 1.7$ K, $B_a^{-\text{full}}$ also splits into two distinct states, one being comparable to B_a^- (highlighted with

an arrow). This behavior is compatible with the interpretation of multiple metastable states, having energies higher/lower than the original nucleation configuration and therefore yielding distinct annihilation fields. Just as it happened with disc1, metastable states become apparent only for negative B and, therefore, only for one specific circulation.

To conclude, we have demonstrated ultra-sensitive nanoSQUID measurements on individual Py nanodiscs. By sweeping the external magnetic field, we can distinguish the processes of vortex nucleation, displacement, and annihilation. By performing multiple measurements at varying temperatures, we also obtained histograms of vortex annihilation. These reveal signatures of ubiquitous multiple metastable configurations. Although disc2 and disc3 had a quite regular circular shape, they likely exhibit defects that lead to different vortex pinning centers. The introduction of intentional asymmetries leads to much more reliable behavior, as demonstrated by disc1, although the presence of multiple metastable states at low temperatures is still evident.

NanoSQUID characterization is, therefore, a powerful tool to differentiate between non-ideal particles (with multiple metastable states) and "ideal" particles, characterized by a single, well-defined minimum energy state with optimal behavior and narrow switching distributions. This can be applied for any kind of magnetization configuration, including textures or single domain magnetic states. For example, one could apply this technique to improve the fabrication method of nanodiscs, aiming to obtain either asymmetric particles with well-defined circulation direction or vortex states with degenerate circulation and polarity.

This work is partly funded and supported by the European Research Council (ERC) under the European Union’s Horizon 2020 research and innovation programme (948986 QFaST), the Spanish MCIN/AEI/10.13039/501100011033 and the European Union FEDER through project PID2022-140923NB-C21, the CSIC program for the Spanish Recovery, Transformation and Resilience Plan funded by the Recovery and Resilience Facility of the European Union, established by the Regulation (EU) 2020/2094, the CSIC Research Platform on Quantum Technologies PTI-001, the Aragón Regional Government through project QMAD (E09_23R) and MCIN with funding from European Union NextGenerationEU (PRTR-C17.I1) promoted by the Government of Aragón. We also acknowledge support by the COST actions FIT4NANO (CA19140) and SUPERQUMAP (CA21144).

I. AUTHOR DECLARATIONS

The authors have no conflicts to disclose.

II. AUTHOR CONTRIBUTIONS

D. García-Pons: Formal Analysis (equal), Investigation (equal), Visualization (equal), Writing/Original Draft Preparation (lead). **J. Pérez-Bailón:** Investigation (equal). **A. Méndiz:** Investigation (equal). **V. Júlvez:** Investigation (equal). **M. Hack:** Resources (equal), Investigation (equal). **K. Wurster:** Resources (equal), Investigation (equal). **R. Kleiner:** Funding Acquisition (equal), Investigation (equal), Methodology (equal), Resources (equal), Supervision (equal). **D Koelle:** Funding Acquisition (equal), Investigation (equal), Methodology (equal), Resources (equal), Supervision (equal), Writing/Review & Editing (equal). **M. J. Martínez-Pérez:** Conceptualization (lead), Formal Analysis (lead), Funding Acquisition (equal), Investigation (lead), Methodology (lead), Resources (equal), Supervision (lead), Validation (lead), Visualization (equal), Writing/Review & Editing (lead)

III. DATA AVAILABILITY

The data that support the findings of this study are available from the corresponding author upon reasonable request.

- ¹T. Shinjo, T. Okuno, R. Hassdorf, K. Shigeto, and T. Ono, “Magnetic vortex core observation in circular dots of permalloy,” *Science* **289**, 930–932 (2000).
- ²A. Wachowiak, J. Wiebe, M. Bode, O. Pietzsch, M. Morgenstern, and R. Wiesendanger, “Direct observation of internal spin structure of magnetic vortex cores,” *Science* **298**, 577–580 (2002).
- ³A. Haldar and A. O. Adeyeye, “Deterministic control of magnetization dynamics in reconfigurable nanomagnetic networks for logic applications,” *ACS Nano* **10**, 1690–1698 (2016).
- ⁴H. Jung, Y.-S. Choi, K.-S. Lee, D.-S. Han, Y.-S. Yu, M.-Y. Im, P. Fischer, and S.-K. Kim, “Logic operations based on magnetic-vortex-state networks,” *ACS Nano* **6**, 3712–3717 (2012).

- ⁵B. Pigeau, G. de Loubens, O. Klein, A. Riegler, F. Lochner, G. Schmidt, L. W. Molenkamp, V. S. Tiberkevich, and A. N. Slavin, “A frequency-controlled magnetic vortex memory,” *Applied Physics Letters* **96**, 132506 (2010).
- ⁶S. R. Bowden and U. J. Gibson, “Logic operations and data storage using vortex magnetization states in mesoscopic permalloy rings, and optical readout,” *Journal of Physics: Conference Series* **200**, 072033 (2010).
- ⁷R. Fermin, J. Yao, K. Lahabi, and J. Aarts, “The unusual distribution of spin-triplet supercurrents in disk-shaped Josephson junctions,” *Superconductor Science and Technology* **36**, 064001 (2023).
- ⁸K. Lahabi, M. Amundsen, J. A. Ouassou, E. Beukers, M. Pleijster, J. Linder, P. Alkemade, and J. Aarts, “Controlling supercurrents and their spatial distribution in ferromagnets,” *Nature Communications* **8**, 2056 (2017).
- ⁹S. Shreya, A. S. Jenkins, Y. Rezaeiyan, R. Li, T. Böhnert, L. Benetti, R. Ferreira, F. Moradi, and H. Farkhani, “Granular vortex spin-torque nano oscillator for reservoir computing,” *Scientific Reports* **13**, 16722 (2023).
- ¹⁰T. Böhnert, Y. Rezaeiyan, M. S. Claro, L. Benetti, A. S. Jenkins, H. Farkhani, F. Moradi, and R. Ferreira, “Weighted spin torque nano-oscillator system for neuromorphic computing,” *Communications Engineering* **2**, 65 (2023).
- ¹¹V. S. Pribiag, I. N. Krivorotov, G. D. Fuchs, P. M. Braganca, O. Ozatay, J. C. Sankey, D. C. Ralph, and R. A. Buhrman, “Magnetic vortex oscillator driven by d.c. spin-polarized current,” *Nature Physics* **3**, 498–503 (2007).
- ¹²S. Wintz, V. Tiberkevich, M. Weigand, J. Raabe, J. Lindner, A. Erbe, A. Slavin, and J. Fassbender, “Magnetic vortex cores as tunable spin-wave emitters,” *Nature Nanotechnology* **11**, 948–953 (2016).
- ¹³Z. Jiang, J. Lim, Y. Li, W. Pfaff, T.-H. Lo, J. Qian, A. Schleife, J.-M. Zuo, V. Novosad, and A. Hoffmann, “Integrating magnons for quantum information,” *Applied Physics Letters* **123**, 130501 (2023).
- ¹⁴B. Z. Rameshti, S. V. Kusminskiy, J. A. Haigh, K. Usami, D. Lachance-Quirion, Y. Nakamura, C.-M. Hu, H. X. Tang, G. E. Bauer, and Y. M. Blanter, “Cavity magnonics,” *Physics Reports* **979**, 1–61 (2022).
- ¹⁵D. Lachance-Quirion, Y. Tabuchi, A. Gloppe, K. Usami, and Y. Nakamura, “Hybrid quantum systems based on magnonics,” *Applied Physics Express* **12**, 070101 (2019).
- ¹⁶M. Trif and Y. Tserkovnyak, “Cavity magnonics with domain walls in insulating ferromagnetic wires,” arXiv:2401.03164 [cond-mat.mes-hall] (2024).
- ¹⁷X.-F. Pan, P.-B. Li, X.-L. Hei, X. Zhang, M. Mochizuki, F.-L. Li, and F. Nori, “Magnon-skyrmion hybrid quantum systems: Tailoring interactions via magnons,” *Physical Review Letters* **132**, 193601 (2024).
- ¹⁸C. Psaroudaki, E. Peraticos, and C. Panagopoulos, “Skyrmion qubits: Challenges for future quantum computing applications,” *Applied Physics Letters* **123**, 260501 (2023).
- ¹⁹S. Khan, O. Lee, T. Dion, C. W. Zollitsch, S. Seki, Y. Tokura, J. D. Breeze, and H. Kurebayashi, “Coupling microwave photons to topological spin textures in Cu_2OSeO_3 ,” *Physical Review B* **104**, 1100402 (2021).
- ²⁰L. Liensberger, F. X. Haslbeck, A. Bauer, H. Berger, R. Gross, H. Huebl, C. Pfleiderer, and M. Weiler, “Tunable cooperativity in coupled spin-cavity systems,” *Physical Review B* **104**, 1100415 (2021).
- ²¹C. A. González-Gutiérrez, D. García-Pons, D. Zueco, and M. J. Martínez-Pérez, “Scanning spin probe based on magnonic vortex quantum cavities,” *ACS Nano* **18**, 4717–4725 (2024).
- ²²M. J. Martínez-Pérez and D. Zueco, “Strong coupling of a single photon to a magnetic vortex,” *ACS Photonics* **6**, 360–367 (2018).
- ²³K. Guslienko, “3d magnetization textures: Toroidal magnetic hopfion stability in cylindrical samples,” *Nanomaterials* **14**, 125 (2024).
- ²⁴A. Fernández-Pacheco, R. Streubel, O. Fruchart, R. Hertel, P. Fischer, and R. P. Cowburn, “Three-dimensional nanomagnetism,” *Nature Communications* **8**, 15756 (2017).
- ²⁵M. J. Martínez-Pérez and D. Koelle, “NanoSQUIDs: Basics & recent advances,” *Physical Science Reviews* **2**, 20175001 (2017).
- ²⁶C. Granata and A. Vettoliere, “Nano superconducting quantum interference device: A powerful tool for nanoscale investigations,” *Physics Reports* **614**, 1–69 (2016).
- ²⁷M. J. Martínez-Pérez, B. Müller, D. Schwebius, D. Korinski, R. Kleiner, J. Sesé, and D. Koelle, “NanoSQUID magnetometry of individual cobalt nanoparticles grown by focused electron beam induced deposition,” *Superconductor Science and Technology* **30**, 024003 (2017).

- ²⁸T. Schwarz, R. Wölbling, C. Reiche, B. Müller, M. Martínez-Pérez, T. Mühl, B. Büchner, R. Kleiner, and D. Koelle, “Low-noise YBa₂Cu₃O₇ nano-SQUIDs for performing magnetization-reversal measurements on magnetic nanoparticles,” *Physical Review Applied* **3**, 044011 (2015).
- ²⁹T. Schwarz, J. Nagel, R. Wölbling, M. Kemmler, R. Kleiner, and D. Koelle, “Low-noise nano superconducting quantum interference device operating in tesla magnetic fields,” *ACS Nano* **7**, 844–850 (2013).
- ³⁰J. Nagel, K. B. Konovalenko, M. Kemmler, M. Turad, R. Werner, E. Kleisz, S. Menzel, R. Klingeler, B. Büchner, R. Kleiner, and D. Koelle, “Resistively shunted YBa₂Cu₃O₇ grain boundary junctions and low-noise SQUIDs patterned by a focused ion beam down to 80 nm linewidth,” *Superconductor Science and Technology* **24**, 015015 (2011).
- ³¹H. Hilgenkamp and J. Mannhart, “Grain boundaries in high- T_c superconductors,” *Reviews of Modern Physics* **74**, 485–549 (2002).
- ³²M. J. Martínez-Pérez, J. Pablo-Navarro, B. Müller, R. Kleiner, C. Magén, D. Koelle, J. M. de Teresa, and J. Sesé, “NanoSQUID magnetometry on individual as-grown and annealed Co nanowires at variable temperature,” *Nano Letters* **18**, 7674–7682 (2018).
- ³³R. P. Cowburn, “Property variation with shape in magnetic nanoelements,” *Journal of Physics D: Applied Physics* **33**, R1–R16 (1999).
- ³⁴K. Y. Guslienko, V. Novosad, Y. Otani, H. Shima, and K. Fukamichi, “Magnetization reversal due to vortex nucleation, displacement, and annihilation in submicron ferromagnetic dot arrays,” *Physical Review B* **65**, 024414 (2001).
- ³⁵M. J. Martínez-Pérez, B. Müller, J. Lin, L. A. Rodríguez, E. Snoeck, R. Kleiner, J. Sesé, and D. Koelle, “Magnetic vortex nucleation and annihilation in bi-stable ultra-small ferromagnetic particles,” *Nanoscale* **12**, 2587–2595 (2020).
- ³⁶A. Garg, “Escape-field distribution for escape from a metastable potential well subject to a steadily increasing bias field,” *Physical Review B* **51**, 15592–15595 (1995).
- ³⁷L. Gunther and B. Barbara, “Quantum tunneling across a domain-wall junction,” *Physical Review B* **49**, 3926–3933 (1994).
- ³⁸J. Kurkijärvi, “Intrinsic fluctuations in a superconducting ring closed with a Josephson junction,” *Physical Review B* **6**, 832–835 (1972).
- ³⁹G. A. Melkov, Y. Kobljanskyj, V. Novosad, A. N. Slavin, and K. Y. Guslienko, “Probing the energy barriers in nonuniform magnetization states of circular dots by broadband ferromagnetic resonance,” *Physical Review B* **88**, 220407 (2013).
- ⁴⁰G. N. Kakazei, M. Ilyn, O. Chubykalo-Fesenko, J. Gonzalez, A. A. Serga, A. V. Chumak, P. A. Beck, B. Laegel, B. Hillebrands, and K. Y. Guslienko, “Slow magnetization dynamics and energy barriers near vortex state nucleation in circular permalloy dots,” *Applied Physics Letters* **99**, 052512 (2011).
- ⁴¹G. Mihajlović, M. S. Patrick, J. E. Pearson, V. Novosad, S. D. Bader, M. Field, G. J. Sullivan, and A. Hoffmann, “Temperature dependent nucleation and annihilation of individual magnetic vortices,” *Applied Physics Letters* **96**, 112501 (2010).
- ⁴²J. P. Davis, D. Vick, J. A. J. Burgess, D. C. Fortin, P. Li, V. Sauer, W. K. Hiebert, and M. R. Freeman, “Observation of magnetic supercooling of the transition to the vortex state,” *New Journal of Physics* **12**, 093033 (2010).
- ⁴³J. A. J. Burgess, D. C. Fortin, J. E. Losby, D. Grombacher, J. P. Davis, and M. R. Freeman, “Thermally activated decay of magnetic vortices,” *Physical Review B* **82**, 144403 (2010).
- ⁴⁴M. Schneider, H. Hoffmann, and J. Zweck, “Magnetic switching of single vortex permalloy elements,” *Applied Physics Letters* **79**, 3113–3115 (2001).
- ⁴⁵R. K. Dumas, T. Gredig, C.-P. Li, I. K. Schuller, and K. Liu, “Angular dependence of vortex-annihilation fields in asymmetric cobalt dots,” *Physical Review B* **80**, 014416 (2009).
- ⁴⁶T. Kimura, Y. Otani, H. Masaki, T. Ishida, R. Antos, and J. Shibata, “Vortex motion in chirality-controlled pair of magnetic disks,” *Applied Physics Letters* **90**, 132501 (2007).
- ⁴⁷L. Exl, S. Bance, F. Reichel, T. Schrefl, H. Peter Stimming, and N. J. Mauser, “LaBonte’s method revisited: An effective steepest descent method for micromagnetic energy minimization,” *Journal of Applied Physics* **115**, 17D118 (2014).
- ⁴⁸A. Vansteenkiste, J. Leliaert, M. Dvornik, M. Helsen, F. Garcia-Sanchez, and B. Van Waeyenberge, “The design and verification of Mumax3,” *AIP Advances* **4**, 107133 (2014).
- ⁴⁹Saturation magnetization $M_{\text{sat}} = 0.86 \times 10^6$ A/m, exchange stiffness $A = 1.3 \times 10^{-11}$ J/m and Gilbert damping $\alpha = 1 \times 10^{-2}$.
- ⁵⁰V. Uhlř, M. Urbánek, L. Hladř, J. Spousta, M.-Y. Im, P. Fischer, N. Eibagi, J. J. Kan, E. E. Fullerton, and T. Šikola, “Dynamic switching of the spin circulation in tapered magnetic nanodisks,” *Nature Nanotechnology* **8**, 341–346 (2013).
- ⁵¹M.-Y. Im, P. Fischer, K. Yamada, T. Sato, S. Kasai, Y. Nakatani, and T. Ono, “Symmetry breaking in the formation of magnetic vortex states in a permalloy nanodisk,” *Nature Communications* **3**, 983 (2012).
- ⁵²F. G. Aliev, A. A. Awad, D. Dieleman, A. Lara, V. Metlushko, and K. Y. Guslienko, “Localized domain-wall excitations in patterned magnetic dots probed by broadband ferromagnetic resonance,” *Physical Review B* **84**, 144406 (2011).